1-1-1999

Comparison of imaging geometries for diffuse optical tomography of tissue

Brian W. Pogue
Dartmouth College

Troy O. McBride
Dartmouth College

Ulf L. Osterberg
Thayer School of Engineering at Dartmouth

Keith D. Paulsen
Thayer School of Engineering at Dartmouth

Follow this and additional works at: https://digitalcommons.dartmouth.edu/facoa

Comparison of imaging geometries for diffuse optical tomography of tissue

Brian W. Pogue, Troy O. McBride, Ulf L. Osterberg and Keith D. Paulsen

Thayer School of Engineering, Dartmouth College, Hanover NH
pogue@dartmouth.edu

Abstract: Images produced in six different geometries with diffuse optical tomography simulations of tissue have been compared using a finite element-based algorithm with iterative refinement provided by the Newton-Raphson approach. The source-detector arrangements studied include (i) fan-beam tomography, (ii) full reflectance and transmittance tomography, as well as (iii) sub-surface imaging, where each of these three were examined in a circular and a flat slab geometry. The algorithm can provide quantitatively accurate results for all of the tomographic geometries investigated under certain circumstances. For example, quantitatively accurate results occur with sub-surface imaging only when the object to be imaged is fully contained within the diffuse projections. In general the diffuse projections must sample all regions around the target to be characterized in order for the algorithm to recover quantitatively accurate results. Not only is it important to sample the whole space, but maximal angular sampling is required for optimal image reconstruction. Geometries which do not maximize the possible sampling angles cause more noise artifact in the reconstructed images. Preliminary simulations using a mesh of the human brain confirm that optimal images are produced from circularly symmetric source-detector distributions, but that quantitatively accurate images can be reconstructed even with a sub-surface imaging, although spatial resolution is modest.

©1999 Optical Society of America

OCIS code: (110.6960) Tomography, (170.3660) Light propagation in tissues, (170.3010) Image reconstruction techniques, (100.3190) Inverse Problems

References and links

1. M. Cope, and D. T. Delpy, "System for long-term measurement of cerebral blood and tissue oxygenation on newborn infants by near-infrared transillumination," Med. Biol. Eng. Comp. **26**, 289-294 (1988).
2. B. Chance, Q. Luo, S. Nioka, D. C. Alsop and J. A. Detre, "Optical investigations of physiology: a study of intrinsic and extrinsic biomedical contrast," Phil. Trans. R. Soc. Lond. B **352**, 707-716 (1997).
3. M. A. Franceschini, K. T. Moesta, S. Fantini, G. Gaida, E. Gratton, H. Jess, H., W. W. Mantulin, M. Seeber, P. Schlag and M. Kaschke, "Frequency-domain techniques enhance optical mammography: initial clinical results," Proc. Nat. Acad. Sci USA **94**, 6468-73 (1997).
4. S. R. Arridge and M. Schweiger, "Sensitivity to prior knowledge in optical tomographic resconstruction," Proc. SPIE **2389,** 378-388 (1995).
5. V. Ntziachristos, M. O,Leary, B. Chance and A. G. Yodh, "Coregistration of images from diffusive wave with other imaging modalities to enhance specificity," in OSA TOPS on Advances in Optical Imaging and Photon Migration II. (OSA publications, Orlando, FL, 1996).
6. J. Chang, H. Graber, P. Koo, R. Aronson, S. S. Barbour, R. L. Barbour, "Optical imaging of anatomical maps derived from magnetic resonance images using time independent optical sources," IEEE Trans. Med. Imag. **16**, 68-77 (1997).
7. B. W. Pogue and K.D. Paulsen, "High resolution near infrared tomographic imaging simulations of rat cranium using apriori MRI structural information," Opt. Lett. **23**, 1716-8 (1998).
8. C. L. Hutchinson, J.R. Lakowicz, and E.M. Sevick-Muraca, "Fluorescence lifetime-based sensing in tissues: a computational study," Biophys. J. **68**, 1574-1582 (1995).
9. J. Chang, H.L. Graber, and R.L. Barbour, "Luminescence optical tomography of dense scattering media," J. Opt. Soc. Am. A **14**, 288-99 (1998).
10. S. R. Arridge, "Forward and inverse problems in time-resolved infrared imaging," in Medical Optical Tomography: Functional Imaging and Monitoring, Ed. G. Muller, (SPIE Optical Eng. Press, Bellingham, WA, 1993) pp. 35-64.

11. D. Boas, "A fundamental limitation of linearized algorithms for diffuse optical tomography," Opt. Express **1**, 404-413 (1997). (http://epubs.osa.org/oearchive/source/2831.htm)

12. H. Jiang, K. D. Paulsen, U. L. Osterberg and M. S. Patterson, "Frequency-domain optical image reconstruction in turbid media: an experimental study of single-target detectability," Appl. Opt. **36**, 52-63 (1997).

13. H. Jiang, K. D. Paulsen, U. L. Osterberg, and M. S. Patterson, "Frequency-domain optical image reconstruction for breast imaging: initial evaluation in multi-target tissue-like phantoms," Med. Phys. **25**, 183-193 (1997).

14. B. W. Pogue, M. Testorf, U. L. Osterberg and K. D. Paulsen, "Instrumentation and design of a frequency-domain diffuse optical tomography imager for breast cancer detection," Opt. Express **1**, 391-403 (1997). (http://epubs.osa.org/oearchive/source/2827.htm)

15. B. W. Pogue, T. O. McBride, J. Prewitt, U. L. Osterberg, and K. D. Paulsen, "Spatially variant regularization improves diffuse optical tomography," Appl. Opt. **38**, (in press) 1999.

16. T. O. McBride, B. W. Pogue, E. Gerety, S. Poplack, U. L. Osterberg, and K. D. Paulsen, "Spectroscopic diffuse optical tomography for quantitatively assessing hemoglobin concentration and oxygenation in tissue," (submitted, 1999), .

17. M. S. Patterson, B. Chance and B. C. Wilson, "Time resolved reflectance and transmittances for the non-invasive measurement of tissue optical properties," Appl. Opt. **28**, 2331-2336 (1989).

18. S. R. Arridge, M. Cope and D. T. Delpy, "The theoretical basis for the determination of optical pathlengths in tissue: temporal and frequency analysis," Phys. Med. Biol. **37**, 1531-1560 (1992).

19. A. H. Gandjbakhche, V. Chernomordik, R.F. Bonner, J. C. Hebden, R. Nossal, "Use of time-dependent contrast functions to discriminate between the scattering and absorption properties of abnormal regions hidden within a tissue-like phantom," Proc. SPIE **2979**, 211-225 (1997).

20. J. A. Moon, R. Mahon, M. D. Duncan and J. Reintjes, "Resolution limits for imaging through turbid media with diffuse light," Opt. Lett. **18**, 1591-1593 (1993).

21. A. H. Gandjbakhche, R. Nossal and R. F. Bonner, "Resolution limits for optical transillumination of abnormalities deeply embedded in tissues," Med. Phys. **21**, 185-91 (1994).

22. D. A. Boas, M. A. O'Leary, B. Chance and A. G. Yodh, "Detection and characterization of optical inhomogeneities with diffuse photon density waves: a signal-to-noise analysis," Appl. Opt. **36**, 75-92 (1997).

23. H. Jess, H. Erdl, T. Moesta, S. Fantini, M. A. Francecshini, E. Gratton and M. Kaschke, "Intensity modulated breast imaging: Technology and clinical pilot study results," Adv. in Optical Imaging and Photon Migration. (OSA publications, Orlando, FL, 1996).

24. S. Fantini, O. Schutz, J. Edler, M. A. Franceschini, S. Heywang-Krbrunner, L. Gotz and H. Siebold, "Performance of N-Images and spectral features in frequency-domain optical mammography," SPIE Technical Abstract Digest. (SPIE Press, San Jose, CA, 1999).

25. Y. Painchaud, A. Mailloux, E. Harvey, S. Verrault, J. Frechette, C. Gilbert, M. L. Vernon and P. Beaudry, "Multi-port time-domain laser mammography: results on solid phantoms and volunteers," SPIE BiOS Technical Abstract Digest. (SPIE Press, San Jose, CA, 1999).

26. J. P. Van Houten, D. A. Benaron, S. Spilman and D. K. Stevenson, "Imaging brain injury using time-resolved near infrared light scanning," Pediat. Res. **39**, 470-6 (1996).

27. M. R. Stankovic, A. Fujii, D. Maulik and D. Boas, "Optical monitoring of cerebral hemodynamics and oxygenation in the neonatal piglet," J. Matern-Fetal Inves. **8**, 71-8 (1998).

28. A. Siegel, J. Marota, J. Mandeville, B. Rosen, and D. Boas, "Diffuse optical tomography of rat brain function," in SPIE Technical Abstract Digest. (SPIE Press, San Jose, CA, 1999).

29. S. Fantini, S. Walker, M. A. Franceschini, M. Kaschke, P. M. Schlag and K. T. Moesta, "Assessment of the size, position, and optical properties of breast tumors in vivo by noninvasive optical methods," Appl. Opt. **37**, 1982-89 (1998).

30. V. Quaresima, S. J. Matcher and M. Ferrari, "Identification and quantification of intrinsic optical contrast for near-infrared mammography," Photochem. Photobiol. **67**, 4-14 (1998).

31. X. Li, J. Culver, J., T. Durduran, B. Chance, A. G. Yodh and D. N. Pattanayak, "Diffraction tomography with diffuse-photon density waves: clinical studies and background subtraction," in Advances in Optical Imaging and Photon Migration. (OSA publications, Orlando, FL, 1993).

32. S. B. Colak, D. G. Papaioannou, G. W. t'Hooft, M. B. van der Mark, H. Schomberg, J. C. J. Paasschens, J. B. M. Melissen and N. A. A. J. van Asten, "Tomographic image reconstruction from optical projections in light-diffusing media," Appl. Opt. **36**, 180-213 (1997).

33. S. R. Arridge and M. Schwieger, "Gradient-based optimisation scheme for optical tomography," Opt. Exp. **2**, 212-226 (1998). (http://epubs.osa.org/oearchive/source/4014.htm)

34. B. J. Tromberg, O. Coquoz, J. B. Fishkin, T. Pham, E. R. Anderson, J. Butler, M. Cahn, J. D. Gross, V. Venugopalan and D. Pham, "Non-invasive measurements of breast tissue optical properties using frequency-domain photon migration," Phil. Trans. R. Soc. Lond. B. **352**, 661-668 (1997).

35. S. R. Arridge and M. Schweiger, "Inverse methods for optical tomography," in Information Processing in Medical Imaging (Springer-Verlag, Flagstaff, AZ, 1993).

36. K. D. Paulsen and H. Jiang "Spatially varying optical property reconstruction using a finite element diffusion equation approximation," Med. Phys. **22**, 691-701 (1995).

37. S. R. Arridge and M. Schweiger, "Image reconstruction in optical tomography," Phil. Trans. R. Soc. Lond. B. **352**, 717-726 (1997).

38. A. Neumaier, "Solving ill-conditioned and singular linear systems: a tutorial on regularization," SIAM Rev. **40**, 636-666 (1998).

39. T. J. Yorkey, J. G. Webster and W. J. Tompkins, "Comparing reconstruction algorithms for electrical impedance tomography," IEEE Trans. Biomed. Eng. **34**, 843-852 (1987).
40. B. W. Pogue, T. O. McBride, C. Nwaigwe, U. L. Osterberg, J. F. Dunn, K. D. Paulsen, "Near-infrared diffuse tomography with apriori MRI structural information: testing a hybrid image reconstruction methodology with functional imaging of the rat cranium," Proc. SPIE 3597 (in press), (1999).

1. Introduction

Diffuse Optical Tomography (DOT) imaging of tissue is emerging as a viable method for non-invasively determining hemoglobin concentration, hemoglobin oxygen saturation, cytochromes, lipids and water in vivo on a centimeter spatial scale. In the past decade, promising applications have emerged in areas such as neonatal and adult cerebral monitoring [1, 2] and breast cancer diagnosis [3]. In addition, DOT may be even more promising when combined with traditional imaging methods [4-7] or when coupled to exogenous contrast agents to monitor tissue function, either through fluorescence or absorption based imaging [2, 8, 9]. One of the limitations in this field of research has been that the rapid advances in technological instrumentation have eclipsed the development of accurate image reconstruction algorithms for diffuse tomography. In this study we focus on one particularly useful image reconstruction algorithm, and apply it in several different imaging configurations in order to evaluate how the source-detector-tissue geometry affects the resulting image.

The use of an appropriate reconstruction algorithm is important because the inverse problem for DOT is inherently ill-posed, and in many cases is ill-conditioned [10], so that standard linear approaches provide limited resolution and contrast inaccuracy [11]. Several iterative reconstruction methods have been tested, and in particular, the Newton-Raphson approach has been shown to provide quantitatively accurate images of the absorption coefficient in a circular tomographic geometry [12-16]. This approach has been developed to characterize breast tumor optical properties in order to diagnose changes in hemoglobin concentration and oxygen saturation of normal and malignant tissues, and is currently being used in our clinical prototype imager.
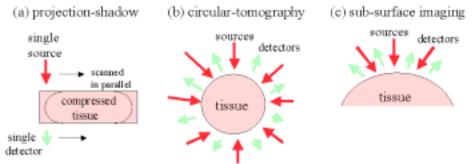

Fig. 1. Schematic of three typical source-detector geometries used in diffuse optical tomography applications. The projection-shadow geometry (a) is used in several optical mammography scanners [3, 23-25], while the circular-tomography geometry (b) is used for both breast and brain imaging [16, 26], as is the sub-surface imaging geometry (c) [2, 27, 28].

There has been considerable study of the type of measurements needed to provide optimal sensitivity in separating the scattering and absorption coefficients in tissue [17-19]. There has also been considerable study of the resolution limits of diffuse tomography [20-22]; however, in general the optimal data types and the resoluton limits are functions of the reconstruction algorithm used to retrieve the images and the source-detector arrangement. Resolution limits calculated from forward solutions may not apply to inversion algorithms which preserve the non-linearity between the internal optical properties of interest and the measured projections at the boundaries. Similarly there has been little investigation of the

geometry and how its boundaries affect the imaging process. As a practical matter, it is quite important to assess the effects that boundaries and source-detector configurations have on the image reconstruction in order to design prototype medical systems. These design considerations are ideally assessed through computer simulations to avoid costly and wasteful construction of clinical prototype systems which may have inherent design flaws. With this goal in mind, we assess geometries which to date represent the most common configurations used for near-infrared imaging and spectroscopy.
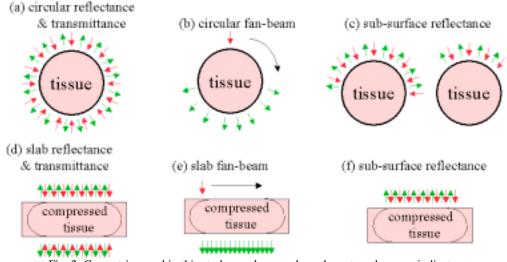

Fig. 2. Geometries used in this study are shown, where the outward arrows indicate detector locations and the inward arrows denote source locations. The geometries include (a) circular reflectance and transmittance imaging which uses circular symmetry for sampling angles (b) circular fan-beam imaging (where the source-detector array is rotated around the tissue), (c) sub-surface tomography which only uses a sub-set of projections from the surface of the tissue, (d) flat slab reflectance and transmittance imaging using maximal sampling from both surfaces, (e) flat slab fan-beam which does not use any reflectance data, and (e) sub-surface imaging with a flat upper surface. Together these six geometries, in various forms, define the possible configurations for imaging tissue with DOT.

The geometries chosen for many laboratory and clinical near-infrared imaging studies fall into three general catagories, which are delineated here as (a) projection-shadow, (b) circular-tomography and (c) subsurface imaging, as shown in Fig. 1. Each of these geometries is being used in clinical investigations for imaging either breast or brain tissues with near-infrared light; yet, there has been little comparison of how the source-detector array geometry will affects the quality of the optical measurements and resulting image. It should be noted that the projection-shadow geometry is generally used for traditional x-ray film style images, where there is no inversion of the data to compute tomographic images [3], and that this geometry does not lend itself to tomographic reconstruction. However, even with this restriction, Fantini *et al.* have been able to retrieve quantitative optical properties from breast tumors using the assumption that the tumor is roughly spherically shaped [29], and this procedure can be even more accurate when multiple projections and multiple wavelengths are incorporated into the analysis [24]. Similarly, Quaresima *et al.* have used this geometry to measure the spectral signature of breast tissue [30]. A variant of this geometry, which exploits a single source location and the angular projections to multiple detectors, has been employed by Li *et al.* [31] to produce backprojection images of breast tissue. Circular tomography has been used successfully in our own studies of hemoglobin based imaging [15, 16] which is being developed for breast cancer diagnosis [32], as well as in work of other investigators for cerebral imaging [26, 33].

In this study, the same DOT image reconstruction algorithm is used to examine: (a) circular full reflectance and transmittance tomography (b) circular fan-beam tomography, (c) sub-surface imaging under a curved boundary, (d) flat slab reflectance and transmittance tomography, (e) flat slab fan-beam tomography, and (f) sub-surface imaging below a flat surface, as shown in Fig. 2. The goal of these tests is to examine the influences of (i) the tissue geometry and (ii) the source-detector configuration upon the recovered image accuracy and quality, and to determine the optimal data collection strategy for characterizing tissue optical properties with this algorithm. The flat slab geometry (Fig. 2 (d) to (f)) is well suited for breast imaging since it provides a configuration similar to x-ray mammography, but it is not clear how the image quality will compare to the more symmetric sampling provided by the circular geometries (Fig. 2 (a) to (c)). We also compare a fan-beam orientation of the detectors where measurements are only recorded on the opposite side to the source (Fig. 2 (b) & (e)), with the full set of projections from all points equally spaced around the tissue (Fig. 2 (a) & (d)). The former orientation is technologically easier to implement because all measurement intensities are within the same range of detector sensitivity, so that parallel implementation is more easily facilitated. However, it is not obvious how this decrease in data affects the resulting optical property distribution, as compared to the full reflectance and transmittance sampling. Finally, subsurface tomography is examined since this is a geometry which is being widely used for near-infrared tomography of brain and breast tissues [2, 28, 34].

2. Theory & Computational Methods

The theoretical details of diffuse optical tomography have been described by several authors, and some good overviews are included in references [35-37]. Forward calculations of diffuse light in tissue can be used to simulate experimental measurements of heterogeneous tissue, and by matching calculated measurements to these simulated experimental measurements an image of the optical properties can be recovered. Since frequency-domain light measurements are used in this work, the frequency-domain diffusion equation is solved with a finite element method. The general form of this equation is:

$$\nabla \cdot D(r)\nabla \Phi(r, \boldsymbol{w}) - [\boldsymbol{m}(r) + i(\boldsymbol{w}/c)]\Phi(r, \boldsymbol{w}) = S_0(r, \boldsymbol{w})$$

(1)

which describes optical fluence rate $\Phi(r,\omega)$ at position r, and frequency ω, given the distribution of absorption coefficient, $\mu_a(r)$ and diffusion coefficient $D(r)$, where c is the speed of light in the medium, and $S_0(r,\omega)$ is the optical source. The diffusion coefficient is usually defined as $D = [3(\mu_s'+\mu_a)]^{-1}$, where μ_s' is the transport scattering coefficient of the medium. This equation is solved with Type III (Robin) boundary condition on a finite element mesh, where all exterior elements are subject to:

$$\Phi(\boldsymbol{x}) + k\nabla \Phi(\boldsymbol{x}, \boldsymbol{w}) \cdot \hat{n} = 0$$

(2)

where ξ is the position on the boundary, $\hat{n}$ is the unit vector normal to the boundary, and k is a calibration constant which has been determined empirically by matching the forward calculations to well controlled experiments [36]. From this solution, we calculate a set of optical measurements, ϕ_i^O, which in this case are phase shift at frequency, ω, and the logarithm of the signal amplitude. While the solution to equation (1) is straightforward given the distribution of μ_a and μ_s', recovering the image distribution of μ_a and μ_s' requires an iterative solution, since equation (1) cannot be directly solved for these values, in part because $\Phi(r,\omega)$ is not known inside the tissue, but only at the discrete points (detector locations) on the boundary.

The Newon-Raphson iterative method for finding the solution of μ_a and μ_s' starts by solving for the minimum of the functional

$$c(\boldsymbol{m}) = (\boldsymbol{f}^C - \boldsymbol{f}^O)^{\mathrm{T}}(\boldsymbol{f}^C - \boldsymbol{f}^O) + l\,F(\boldsymbol{m})$$

(3)

where we use μ to represent both μ_a and $\mu_s^{/}$ as the set of coefficients, and $F(\mu)$ is an arbitrary functional which smooths the solution to reduce the ill-posed nature of the eventual matrix inversion [38]. Minimizing (3) by taking the derivative and setting it equal to zero, followed by expansion of the solution in a Taylor's series [39], leads to,

$$0 = (\boldsymbol{f}^C - \boldsymbol{f}^O)^{\mathrm{T}}\mathbf{J} + \Delta\boldsymbol{m}(\mathbf{J}^{\mathrm{T}}\mathbf{J} + l\mathbf{I}) + \dots$$

(4)

where the elements of $\mathbf{J}$ are given by $\partial\phi_i / \partial\mu_k$, for observation i, at each pixel position k. In this derivation, the higher order derivatives of ϕ are assumed to be negligible, and $F(\mu)$ is chosen to result in the classical Tikhonov regularized formulation [38]. Finally the iterative solution becomes,

$$\Delta\boldsymbol{m} = (\boldsymbol{f}^C - \boldsymbol{f}^O)^{\mathrm{T}}\mathbf{J}[\mathbf{J}^{\mathrm{T}}\mathbf{J} + l\mathbf{I}]^{-1}$$

(5)

where $\Delta\mu$ is the update for the current estimate of μ. The values of ϕ^C and J are calculated using the current estimate of μ. In practice we have found that the regularization parameter can be varied between iterations for improved reconstruction, and can be varied spatially to compensate for some geometrical artifacts induced during the reconstruction process [15].

In the following simulations, the forward and inverse calculations have been carried out with a finite element solution which has been tested extensively in previous papers [The simulated measurements were calculated on the same meshes that were used for the reconstructions and 1% random gaussian-distributed noise was added to both the real and imaginary components of the measurements in order to simulate true source-detector noise. All reconstructions were carried out with the same regularization parameter, and 5 iterations have been used in each case. Each iteration requires approximately 1.5 minutes on a 200 MHz desktop computer running Windows NT. In all the reconstructed images shown in this paper, the dimensions of the field are shown in millimeters on the x and y axes of the figure.

3. Results

3.1 Imaging Fields with a Single Localized Target

A series of forward and inverse simulations have been completed for each geometry shown in Figure 2. The overall goal has been to maintain a uniform test between geometries and determine those geometries which introduce significant artifacts into the reconstruction by the nature of the boundaries and source-detector configuration. There are an infinite number of possible tests which could be used in each of these geometries, but we have chosen to begin with a physiologically relevant contrast in a tumor sized target. In all cases the background optical properties were fixed at $\mu_a = 0.01$ mm^{-1} and $\mu_s^{/} = 1.0$ mm^{-1}, and a simulated target within the field has been included with a radius of 10 mm and optical properties of $\mu_a = 0.02$ mm^{-1} and $\mu_s^{/} = 1.0$ mm^{-1}. In each geometry the target is moved around to positions within the imaging field which have different levels of symmetry, potentially affecting the resulting image qualtity.

3.1.1 Circular Reflectance and Transmittance Imaging

A circular mesh was used with 221 nodes in the coarse calculation of the Jacobian and matrix inversion as shown in equation (5), and 425 nodes in the fine mesh were used for solution of equation (1). A circularly symmetric configuration of 16 sources and 16 detectors was used in the solution, providing a data set of 256 projections, as shown in Fig. 2 (a). The field was 86 mm in diameter, with the sources and detectors spaced symmetrically around the periphery, with one every 11.25 degrees alternating between source and detector. The test target was moved to different radial positions between the center and the edge of the field to

examine the quality of the reconstructions which are presented in Fig. 3. Because this simulation has circular symmetry, no other target locations are needed to characterize the image field.
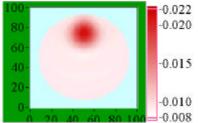

Fig. 3. Reconstructed set of images (video sequence) of the test target at different vertical positions within the circular mesh, using source-detector geometry in Fig. 2 (a) with a circularly symmetric distribution of 16 source and 16 detectors for reflectance and transmittance imaging. The color bar on the right is in absorption coefficient units of mm^{-1}.

3.1.2 Circular Fan-Beam Imaging

This orientation of source and detectors is shown in Fig 2(b), where for each source location, 8 detectors were used on the opposite side of the phantom. Then the source and locations of the 8 detectors are rotated around the phantom to 16 different sets of projections through the phantom, resulting in 128 measurements of phase shift and signal amplitude. The spacing of field and source-detectors was otherwise identical to Fig. 3. This geometry has the experimental advantage that the signal intensity at all 8 detectors is within an order of magnitude in variation, so that large changes in the dynamic range of the detectors is not encountered. This data set can be considered as a sub-set of the data available in the previous case of full reflectance and transmittance with the near-source detectors removed. The location of the test target was varied in the object field between the center and the top edge. Again, since the sources and detectors are located in circularly symmetric orientations, this set of target locations is sufficient to characterize the entire image field for this size and shape of object, as shown in Fig. 4.
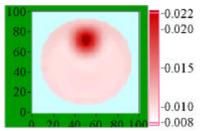

Fig. 4. Reconstructed set of images (video sequence) showing the test target at different vertical positions within the circular mesh, using the fan beam geometry with 16 sources transmitting to 8 detectors. The color bar on the right is in absorption coefficient units of mm^{-1}.

3.1.3 Sub-surface Imaging – Curved Boundary

Near-infrared imaging is confounded by the high attenuation of the light in tissue, such that in practice, it is often not possible to detect light reliably through tissue samples thicker than 10 cm. Also, the instrumentation for imaging through tissue less than 5-6 cm can be much simpler, more robust and less expensive than for thicker tissues [28]. For this reason, many investigators have focused on sub-surface imaging applications where the sources and detectors are located on the same tissue surface and are arranged to probe the interior of the tissue. This sub-surface tomography can be performed on a curved tissue such as a neonate or adult head and female breast. These tissues are well simulated with a finite element

solution assuming that the boundary curvature is known and can be input into a finite element mesh. If the light does not sample deeply into the tissue, the tissue boundary can be approximated by a simple circular mesh which has a matching radius of curvature. In the next series of simulations, this sub-surface imaging method has been investigated using the same circular mesh as above, but with only the source and detector locations on the upper region of the mesh activated. Both situations illustrated in Fig. 2 (c) were examined including: 8 sources-8 detectors (8x8) and 4 sources-4 detectors (4x4). The imaging field is symmetric about the center of the source-detector array, so that the image quality is adequately assessed by translating the test object vertically down from the upper surface, as shown in Fig. 5.
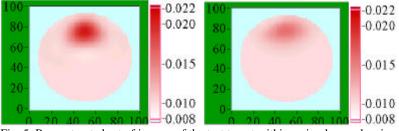

Fig. 5. Reconstructed set of images of the test target within a circular mesh using the sub-surface orientation with (a) 8 sources and 8 detectors in an arc, and (b) 4 sources and 4 detectors in a smaller arc on the surface (as shown in Fig. 2(c)). Color bar at right is in absorption coefficient units of mm^{-1}.

3.1.4 Slab Reflectance and Transmittance Imaging

The slab geometry mimics x-ray mammography and minimizing the thickness of tissue that must be imaged, potentially allowing the use of less sensitive, but more stable, solid state detectors. Light signals from the tissue can be recorded from both the upper surface near the source, as well as transmitted through the slab. This geometry is referred to here as slab reflectance and transmittance imaging, and is examined in the same set of simulations as the circular geometry described in the previous sections. One major difference from the circular geometry is the lack of symmetry, so that the response of the imaging field will likely vary with both vertical and horizontal position. Thus, in order to fully characterize the image plane, the test object has been translated along three lines: vertically through the center, horizontally through the center, as well as horizontally along the upper surface, as shown in Fig. 6. In the slab mesh, 260 nodes were used in the coarse calculation of the Jacobian in equation (5) and 380 nodes were used in the fine mesh solution of equation (1). The source detector arrangement was as shown in Fig. 2(d), with 5 mm between each source and detector.
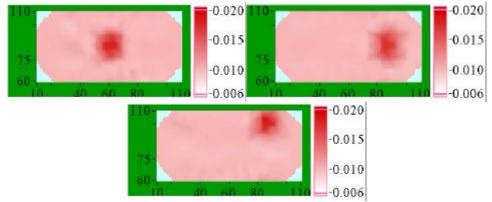

Fig. 6. Reconstructed set of images of the test target at different (a) vertical positions (b) lateral positions along the central line, and (c) lateral positions along

the surface, using the slab reflectance and transmittance geometry of sources and detectors as shown in Fig. 2 (d).

3.1.5 Slab Fan-Beam Imaging

The fan-beam geometry for slab breast imaging is an obvious choice since it can involve the use of parallel detection through a CCD or other parallel detectors, which are highly stable and provide robust detection.   The simplicity of translating the source across the upper surface of the tissue is beneficial, but it is not clear how the loss of reflectance information will affect the reconstructed images of the tissue interior. The geometry used in this section was as shown in Fig 2.(e), with 5 mm between neighbouring fibers. In these simulations, the asymmetry is similar to the previous section, so that the same set of simulations were carried out to examine the imaging field sensitivity, shown in Fig. 7.
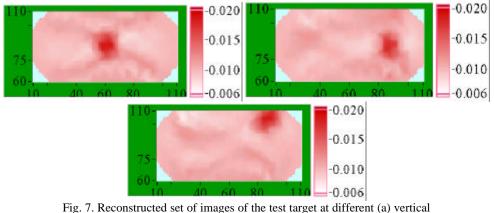

Fig. 7. Reconstructed set of images of the test target at different (a) vertical positions (b) lateral positions along the central line, and (c) lateral positions along the surface similar to those in Fig. 6, using fan-beam slab imaging.   Color bar at right is in absorption coefficient units of mm^{-1}.

3.1.6 Sub-surface Imaging – Flat boundary

The flat boundary is perhaps one of the most often used geometries for near-infrared sub-surface imaging because it is simple, readily available clinically in many body locations, and lends itself to analytic reconstruction methods.   This geometry was tested here with 16 sources and 16 detectors all located on the upper surface of the tissue volume producing 256 projections through the medium, spaced alternating at in Fig. 2 (f), with 2.5 mm between each.   The high number of sources and detectors was employed to provide the best performance that we could obtain in this geometry.   The test object was translated vertically down from the surface, as with the sub-surface imaging on the circular mesh (*Section 3.1.3*), with the results shown in Fig. 8.
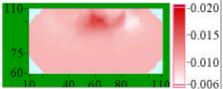

Fig. 8. Reconstructed set of images where the test target was translated vertically from the middle of the tissue volume (25 mm down) up to the surface, using 16 sources and 16 detectors alternated and equally spaced along the upper surface of the region, as illustrated in Fig. 2 (f).

3.2 Comparison of Geometries – Contrast and Noise

The above simulations do not completely define the characteristics of the imaging geometry and slight improvements can be achieved for individual cases by adjusting the regularization parameter both during an iteration and spatially-distributed across the imaging plane [15]. Nonetheless comparing the reconstructed peak values in the target zone and the typical noise in the homogeneous background of the image are useful measures of the ability to reconstruct objects accurately. In Fig. 9 (left-top graph) the reconstructed peak values for each target are plotted for changes in vertical position through the image plane. Fig. 9 (right-top graph) is a plot of the standard deviation of the noise within what should be the homogeneous regions of the resulting images. In the peak absorption coefficient, if the value is within 20% of the original target it is considered acceptable. This criterion is simply based upon the typical variations in reconstructed properties observed in previous studies [16].
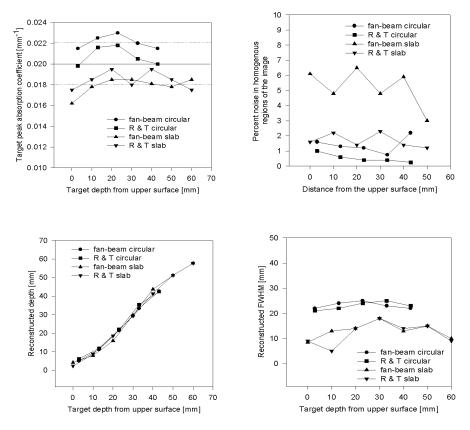

Fig. 9. Calculated (left-top graph) peak absorption coefficient values for the object at different positions within the simulated phantoms, and (right-top graph) reconstructed noise in the background region of the image measured by sampling of random regions of interest outside the target zone. The true value in the first graph is shown with a solid horizontal line, and the 20% region of acceptability is defined by the dotted lines. Calculated (left-bottom graph) target location as a depth from the upper surface, and (right-bottom graph) the calculated target full width at half maximum (FWHM) height as a function of depth in the medium, here taken as an average of the lateral and vertical directions.

A comparison of the three subsurface imaging geometries is shown in Fig. 10, using the same criteria of acceptable peak reconstruction value, as shown in Fig. 9. The reconstructed peak absorption coefficient values for the single targets are shown in Fig. 10 (left-top) as a

function of the depth into the medium, and typical noise values are plotted in Fig. 10 (right-top). In this case, the only geometry which was able to reconstruct accurate absorption coefficient values over a moderate range of depths was with the 8x8 circular arc and the reconstructed peak values decrease significantly with depth for all three sub-surface imaging geometries.
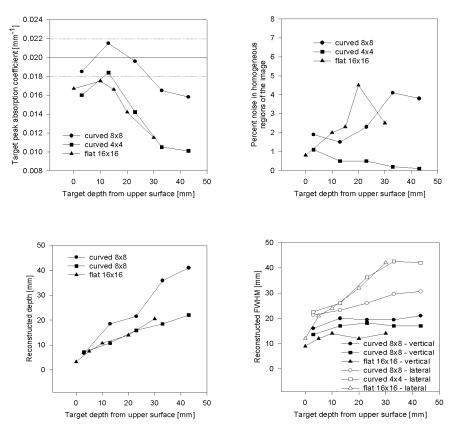

Fig. 10. Calculated (left-top graph) peak absorption coefficient values for the target zone at different positions within the simulated phantoms, and (right-top graph) reconstructed noise in the homogeneous background region of the image outside the target zones. Calculated (left-bottom graph) target location as a depth from the upper surface, and (right-bottom graph) the calculated target full width at half maximum (FWHM) height as a function of depth in the medium, measured here both in the lateral and vertical directions.

3.3 Imaging Fields with Multiple Targets

In addition to imaging single objects it is important to recover more complicated distributions, so an additional test has been constructed to compare multiple targets in the circular and slab geometries. The test field contained three targets positioned at different depths, as illustrated in the circular and slab schematic images in the left column of Fig. 11. In this case, two targets were 20 mm in diameter with one in the exact center of the field and one on the right edge at the surface (and upper region in the slab case). The third target had a 10 mm diameter and was located on the left edge of each image (and towards the bottom surface in the slab). All three targets presented a contrast of 2:1 in absorption. The resulting reconstructions for reflectance and transmittance geometries are shown in the middle column while fan-beam reconstructions are contained in the right column of Fig. 11. The image

quality of the two sub-surface geometries is clearly limited in depth resolution, so that the same tests have not been applied to these cases. Therefore, a separate multi-target test consisting of two sub-surface objects, both 10 mm diameter and 2:1 in contrast but with one on the surface and the other 5 mm below, was used to compare these sub-surface configurations, as shown on the left of Fig. 12. The reconstructed images using the 4x4 and 8x8 circular arcs and the 16x16 flat slab are presented in the right columns of the figure.
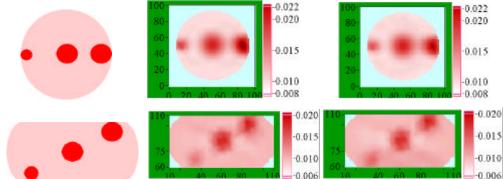

Fig.11. Reconstructed images of three localized targets within a homogeneous background field, (schematics shown in the left column) using geometries of (upper middle) circular reflectance & transmittance (upper right) circular fan-beam, (lower middle) slab reflectance & transmittance, and (lower right) slab fan-beam. The test targets (left) were all 2:1 absroption contrast from the background, and the two on the right were 20 mm diameter, while the one on the left is 10 mm in diameter.
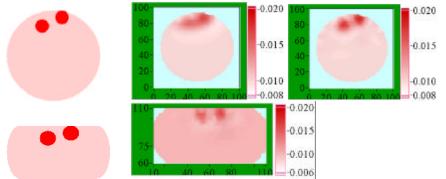

Fig. 12. Reconstructed images of the test fields (shown in the left colum) are displayed at right. The test fields contained two 10 mm diameter objects with one on the surface and the other 5 mm below the surface. In the top row, the middle image shows the result of the 4 source-4 detector array while the right image shows the result from the 8 source-8 detector array. In the bottom row, the result from the slab geometry is shown using the 16 source-16 detector array.

3.5 Imaging Fields with Layered Structure

A third test was performed to examine the influence of geometry on the ability to recover a layered structure within the medium. In this situation, the field consisted of three concentric layers of differing absorption coefficient with a single circular inhomogeneity located within the layers. The schematic of the test object is shown in Fig. 13 in the left column, with the circular test field in the upper row, and the corresponding slab test field in the lower row. The reconstructed images using the full reflectance & transmittance and fan-beam approaches are shown in the center and right columns of the figure, respectively. Interestingly, in all cases the circular target could be localized and reconstructed to within

20% of the true value, but the layered structure near the surface was best recovered in the circular geometry. In particular, the full reflectance and transmittance array provided a better reconstruction of the layered structure than did the fan-beam approach, while both slab approaches were dominated by artifacts in the background.

In Fig. 14, the same layered test fields as in Fig. 13 were used to evaluate the sub-surface imaging geometries. These methods were not expected to reconstruct the lower regions of the phantom, but the upper layers and the presence of the object can be partially reconstructed in all cases. The 4x4 detector strategy and the slab 16x16 scheme cannot fully discriminate the object from the layers, while the 8x8 arc geometry can partially reconstruct both the layers and the presence of the object.
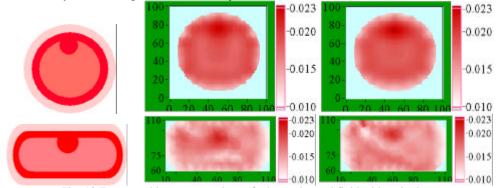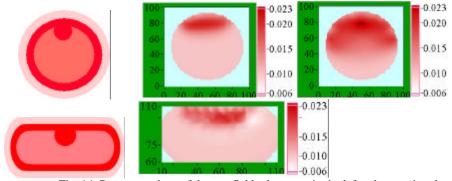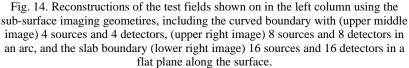

Fig. 13 Tomographic reconstructions of a layered tested field with a single target included for both circular (top row) and slab (bottom row) geometries, with two 5 mm thick layers of $\mu_a = 0.01$ and $\mu_a = 0.02$, with the interior at $\mu_a = 0.015$ mm^{-1}, and a 20 mm diameter object at $\mu_a = 0.02$ mm^{-1}. The images in the left column represent the test field, while the middle row of images show the full reflectance and transmittance images, and the right column of images show the fan-beam images.

Fig. 14. Reconstructions of the test fields shown in the left column using the sub-surface imaging geometires, including the curved boundary with (upper middle image) 4 sources and 4 detectors, (upper right image) 8 sources and 8 detectors in an arc, and the slab boundary (lower right image) 16 sources and 16 detectors in a flat plane along the surface.

3.5 Application to Irregular Tissue Geometries – Cerebral Hemoglobin Imaging

In an effort to consider these source-detector arrangements in a more realistic geometry, a magnetic resonance image of a human brain was segmented into a finite element mesh (shown in Fig. 15) and used to simulate imaging with the three source-detector geometries (i) fan beam (ii) reflectance and transmittance and (iii) sub-surface imaging. The head size was scaled to that of a neonate, and typical optical properties were applied to the skin, bone, grey

matter and white matter [7,33]. A 15 mm diameter inclusion was added in the upper left of the brain with $\mu_a = 0.03$ mm^{-1}, representing a 50% increase from the grey matter, and a 200% increase from the white matter. The initial guess for the image was a homogeneous head shape with $\mu_a = 0.01$ mm^{-1}. The inclusion was observed in all reconstructed images with a peak value within 10 % of the true value, indicating that it can be successfully characterized with all three source-detector geometries using this algorithm. Interestingly, none of the imaging geometries could discriminate the white matter structure from the grey matter, but the full reflectance and transmittance method was able to recover the skull optical properties accurately, as was the sub-surface imaging geometry. Also the fan-beam approach produced significant artifact into the image, as a ringing structure. Surprizingly the fan-beam approach recovers the presence of the object clearly, albeit not at a accurate contrast level.
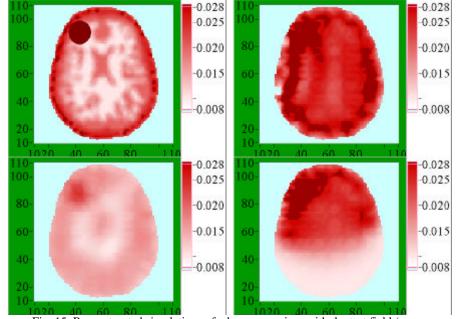

Fig. 15. Reconstructed simulations of a human cranium with the test field (upper left), showing absorption coefficients of skin, $\mu_a = 0.01$, skull, $\mu_a = 0.025$, grey matter, $\mu_a = 0.02$, and white matter, $\mu_a = 0.01$ mm^{-1}, with a fixed scattering coefficient of $\mu_s' = 1.0$ mm^{-1}. An artificial inclusion having $\mu_a = 0.03$ was included in the upper left of the test field. The reconstructed images are shown using full reflectance and transmittance imaging (upper right), fan beam imaging (lower left), and 8x8 sub-surface imaging with the detectors in an arc around the upper half of the head (lower right). Note that the sub-surface geometry is not expected to recover properties in the lower half of the image.

4. Discussion

4.1 Geometry Effects in the Reconstructed Image

Determining the optimal source-detector and tissue geometry is not as simple of a task as it might first appear because of the interplay between theoretical performance and practical constraints, so that some theoretically optimal designs must be considered in light of experimental limitations. As a result, all of these issues cannot be fully characterized by the simple simulations contained in this paper. Also, the reconstruction algorithm could be better tailored to any of the specific geometries than in its present generalized form, by altering the regularization scheme to improve the reconstruction to provide a more homogeneous solution across the imaging field [15]. In the cases shown here, the regularization parameter was

chosen to provide optimal reconstructions, through a series of trials, so that the images shown here are our best versions. However, even with these uncertainties about regularization, there are some reconstruction results which are indicative of the measurement data quality which can be used to evaluate and compare the individual geometries. Our goal has been to determine if the geometry significantly inhibits the ability to accurately reconstruct optical properties, or if the geometry adds artifacts to the resulting image which are not easily avoided.

When comparing reconstruction geometries, it would be ideal to have the same number of measurements in the data set, so that changes in geometry are not confounded by changes in the conditioning of the matrix; however, in practice the physical size of the source and detector fibers can limit the number of possiblilities which are available for a given geometry. For example, in the circular geometry, the minimum tissue diameter and the diameter of the fibers dictates the number of sources and detectors that are possible. For these reasons, we have chosen to compare geometries and source-detector arrangements which are physically realistic, while trying to maintain the maximum number of measurements in each data set. The fan-beam and sub-surface imaging schemes can be thought of as sub-sets of the data measured in the full reflectance and transmittance mode, so that it is not surprising that there is some loss of image resolution with each of these two methods. We have also constrained the problem to be 2-dimensional in these cases, however based upon previous experience we anticipate that similar results are obtained in 3-dimensions. Also fully 3-dimensional reconstruction is inherently difficult to interpret, and often requires separation into 2-d slices in order to fully evaluate the image quality. For these reasons, the 2-dimensional images shown here are thought to be representative of the available image quality for each respective geometry.

4.2 Single Targets

In the video sequences of Figs. 3 to 8, the object is localized accurately in all cases, and is close to the original true value at most locations (as shown in Fig. 9). Small deviations from the true value can be compensated with changes in the regularization parameters [15], but large deviations from the true value which are accompanied by significant noise in the image cannot generally be eliminated. An example of this phenomenon is observed in Fig. 7, where the fan-beam slab reconstructions show a marked increase in noise within the image, while there is no decrease in the recovered peak height of the target. This noise is likely due to the decreased angles of projection which are used to sample the field, producing regions within the image which cannot be well charaterized by the solution to the inverse problem. Maximizing the number of different angular projections through the field is likely the best way to improve the accuracy of the inverse solution.

Recovering images in the sub-surface imaging geometry is more challenging than with full tomographic methods, and this is expected since the tissue cannot be sampled as effectively ina purely reflectance mode. The most important observation from the data in Fig. 9 is that the true value of the object is not easily recovered without being able to sample measurements in an arc around the tissue sample, as is the case with the 8 source-8 detector array in the circular geometry. By adjusting the regularization parameters, it would be possible to reconstruct the peak values for all three geometries used here, as long as the depth of the target is not lower than 20-30 mm. At depths below 30 mm, the photon paths cannot sample the target effectively. In general as the target is lowered into the medium, the reconstructed peak value will decrease.

4.3 Multiple Targets

When multiple targets are present as in Figs. 11 & 12, the circular geometries tend to over-reconstruct targets on the periphery. This problem can be compensated with a radial variation in the regularization parameter [15]. The slab geometries do not recover the smaller test target as well as their corresponding circular geometries. There are no clear

differences between the fan-beam style versus the full sampling of reflectance and transmittance, other than the expected increase in background noise in the fan-beam case. The subsurface imaging method suffers from a field sensitivity which decreases with depth into the tissue, such that lower lying objects are not as strongly reconstructed as objects immediately at the surface.

4.4 Layered Fields

When layered test fields are used, there is serious degradation of the image quality in the case of the slab geometry (Fig. 13), whereas both circular geometries were able to provide reasonable images of the subsurface ring and the upper inclusion. Again, the full reflectance and transmittance circular mode provided a slightly more accurate reconstruction of the test field than the fan-beam circular mode. Note that the layer in the circular fan beam reconstruction is closer to the center than in the original test field (Fig. 13). All three sub-surface imaging method are able to reconstruct parts of the layered structure, but only the 8x8 detection method is sufficient to recover the inclusion quantitatively below the layer. It is likely important to ensure that the diffuse projections sample below the suspected inclusion in order to produce an accurate reconstruction of the target. This layered test field is important, since almost all in vivo tissues have a complex layered structure near the surface that may not be clearly resolved unless a circular reflectance and transmittance geometry is used.

4.5 Cranial Imaging

For the cranial images in Fig. 15, the complex structure between white and grey matter is not well resolved, which agrees with the observations of other investigators [33]. The location of the skull is well resolved with the full reflectance and transmittance method, but the interior is not. The sub-surface imaging geometry provides a method sufficient to quantify the optical properties of the inclusion. The fan-beam imaging appears to image asymmetric regions, such as the inclusion quite well but cannot recover the skull or brain details at all. In general, the white/grey matter variations which appear on a sub centimeter scale cannot be resolved; however, larger changes in the optical properties, such as the artificial target in the upper left, can be resolved given. It is also likely that absolute changes in the optical properties can be better resolved than the absolute magnitude of the property itself, whereas only the latter case has been tested here. Further study is needed to determine the increase in image quality which is possible with incorporation of MRI-derived initial guesses of the optical property distribution, and other enhancments of the reconstruction process through adaptive spatial regularization or constraints [7, 40].

5. Conclusion

In general, increasing the number of measurements improves the quality of the reconstructed images and the image accuracy. Care must be taken to ensure that the projections used provide a homogenous sampling of the entire tissue region of interest, and that the projections maximize the number of angles over which measurments are recorded. The ability to resolve objects improves as the distribution of angular projections increases through the sample; so, the maximum angular coverage of a tissue results from the circular geometry with full sampling of the reflectance and transmittance light, which is demonstrated to have the best image quality in these simulations. The technological simplification of using a fan beam approach is attractive and comes at only a modest decrease in image quality, so this may provide the most practical method for optical imaging. The fan beam approach produces measurments which are all near the same order of magnitude in intensity so that variable attenuation is not required in the data acqusition system.

A comparison of slab-geometry imaging to circular-geometry imaging with single objects does not demonstrate a major difference in the image quality, but the ability to image layered objects with the slab-geometry was seriously compromised. From these simulations,

we anticipate that the slab geometry is not well suited to imaging layered structures, and this may be due to the relatively few projections at varying angles through the layers which exist. Sub-surface imaging produces the lowest quality images, but is able to quantify absorbing perturbations near the surface. Objects lower than 2 cm are not likely to be imaged accurately by subsurface methods unless the overlying surface is curved. Curved surfaces allow the light projections to probe deeper into the tissue and can provide accurate images of sections of a tissue. The image quality for all geometries presented in this paper is compromised by the generality of the inversion algorithm, so that some improvements can potentially be incorporated for each particular geometry through spatially distributed regularization methods or adaptive regularization [15].